nature structural & molecular biology

Structural basis for the unfolding of anthrax lethal factor by protective antigen oligomers

Geoffrey K Feld[1,4], Katie L Thoren[1,4], Alexander F Kintzer[1], Harry J Sterling[1], Iok I Tang[1], Shoshana G Greenberg[2], Evan R Williams[1,3] & Bryan A Krantz[1–3]

The protein transporter anthrax lethal toxin is composed of protective antigen (PA), a transmembrane translocase, and lethal factor (LF), a cytotoxic enzyme. After its assembly into holotoxin complexes, PA forms an oligomeric channel that unfolds LF and translocates it into the host cell. We report the crystal structure of the core of a lethal toxin complex to 3.1-Å resolution; the structure contains a PA octamer bound to four LF PA-binding domains (LF_N). The first α-helix and β-strand of each LF_N unfold and dock into a deep amphipathic cleft on the surface of the PA octamer, which we call the α clamp. The α clamp possesses nonspecific polypeptide binding activity and is functionally relevant to efficient holotoxin assembly, PA octamer formation, and LF unfolding and translocation. This structure provides insight into the mechanism of translocation-coupled protein unfolding.

Protein secretion and degradation are essential cellular processes that allow for protein trafficking, organelle biogenesis, protein quality control and cell-cycle regulation[1–3]. Because folded proteins are thermodynamically stable under typical conditions, these processes often require complex, energy-consuming molecular machines[3–6], which catalyze a series of unfolding and translocation reactions[7–13]. Anthrax toxin[5,14], a three-protein virulence factor secreted by *Bacillus anthracis*, is an example of such a transmembrane protein-delivery system (**Supplementary Fig. 1**). This bacterial toxin follows the classical two-component AB paradigm, in which the A component is an active enzyme that localizes to and enters cells by forming complexes with the cell-binding, or B, component. Anthrax toxin is composed of two A components, LF (91 kDa) and edema factor (EF, 89 kDa), and one B component, PA (83 kDa). Therefore, two different toxic complexes can form: lethal toxin (LT, consisting of PA plus LF) and edema toxin (ET, consisting of PA plus EF). LT (which we focus on herein) causes macrophage lysis[15], immune-system suppression[16] and death[14].

For LT to inflict its cytotoxic effects, PA and LF must assemble into active holotoxin complexes that can translocate LF into host cells (**Fig. 1a**). Proteases present either on host-cell surfaces or in blood serum potentiate LT assembly by proteolytically nicking PA, yielding $_nPA$[17–19]. Dissociation of a 20-kDa N-terminal fragment from $_nPA$ exposes LF-binding sites, permitting its assembly with LF. The resulting LT complex contains multiple copies of LF bound to either a ring-shaped PA homoheptamer, PA_7 (refs. 18–21), or homooctamer, PA_8 (ref. 19). Octameric PA forms more robust LT complexes than heptameric PA under physiological conditions[22]. The crystal structures of the individual PA and LF monomers[20,23] and the assembled PA heptamer[24] and octamer[19] are known. However, an atomic-resolution X-ray crystal structure of a lethal toxin co-complex has not been described.

After the LT complex is endocytosed, the PA oligomer transforms into a transmembrane, β-barrel channel[25] through which LF translocates to enter the cytosol. Because of the narrowness of the channel, LF unfolds during translocation. The acidic endosomal pH conditions required for toxin action[15] not only aid in the destabilization of LF[26] but also drive further LF unfolding[9] and translocation by means of a proton-motive driving force[7]. This driving force comprises a proton gradient (ΔpH) and membrane potential ($\Delta\psi$). Efficient coupling of the ΔpH requires a catalytic active site in the channel, called the ϕ clamp, composed of a narrow ring of phenylalanine residues[7,8]. The ϕ clamp forms a narrowly apposed substrate-clamping site in the central lumen of the PA channel[8], and it allows the channel to catalyze unfolding[9] and translocation[8], presumably by forming transient interactions with the unfolded translocating chain[8].

Many, but not all, protein processing machines that translocate, unfold and/or refold proteins use analogous polypeptide clamping features to denature a protein and engage with its unfolded structure. The features that bind to unstructured or unfolded polypeptides include hydrophobic and aromatic pore loops[8,11,27–29], polypeptide clamping sites[8,30] and other substrate-binding clefts or adapters[31–33]. Some of these machines use tandem polypeptide binding sites[8,9,31]: one site is a substrate docking site, and it feeds into a second, hydrophobic site found deeper within the pore. Questions surround the mechanisms of action of these clamping sites and their interactions with unfolded substrates. How do these sites unfold proteins? How do they process the wide chemical complexity and configurational

[1]Department of Chemistry, University of California, Berkeley, California, USA. [2]Department of Molecular & Cell Biology, University of California, Berkeley, California, USA. [3]California Institute for Quantitative Biosciences, University of California, Berkeley, California, USA. [4]These authors contributed equally to this work. Correspondence should be addressed to B.A.K. (bakrantz@berkeley.edu).

Received 15 June; accepted 7 September; published online 31 October 2010; doi:10.1038/nsmb.1923

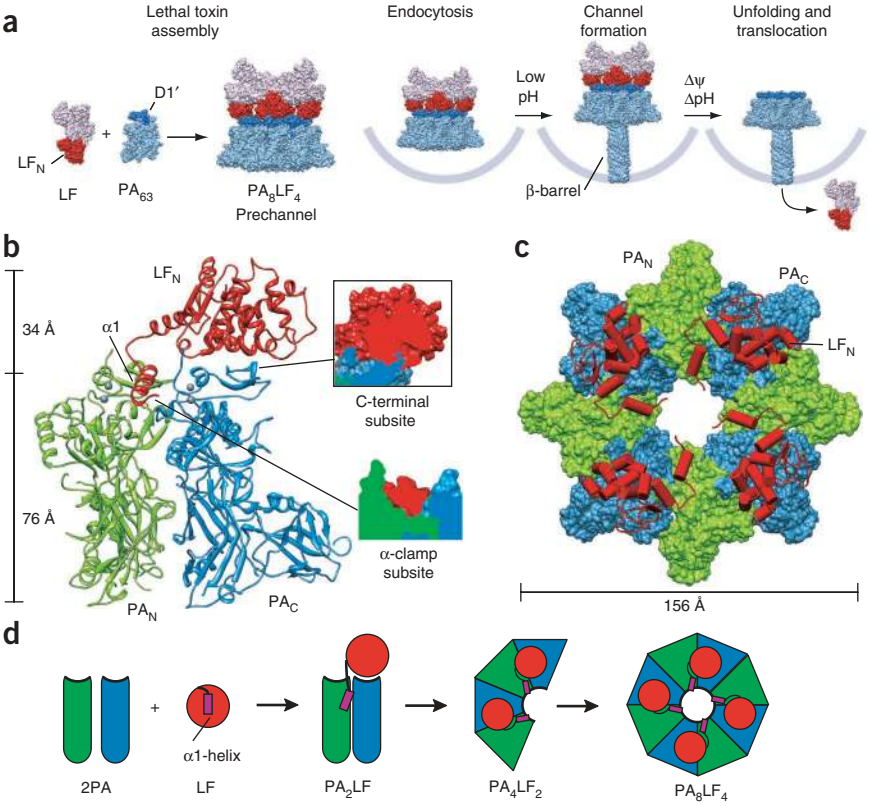

Figure 1 Structure of LF's PA-binding domain in complex with the PA octamer. (**a**) An overview of LT assembly and LF translocation. LF (PDB 1J7N[23] (pink) with LF_N (red)) and a PA_{63} subunit (PDB 3HVD[19] (light blue) with D1′ (blue)). LF and PA_{63} assemble into either heptameric (PA_7LF_3) or octameric (PA_8LF_4) LT complexes. The PA_8LF_4 complex depicted was verified by mass spectrometry (**Supplementary Fig. 2a**) and is based upon structural data presented herein. LT is endocytosed; the endosome is acidified, causing PA to form a β-barrel channel[25]; LF translocates through the channel under a ΔpH/Δψ-driving force to enter the cytosol; and LF then disrupts normal cellular physiology by cleaving mitogen-activated kinase kinases[50]. (The channel depicted is a model intended for illustration purposes only). (**b**) Left, ribbon depiction of the PA_2LF_N ternary complex. PA_C (chain A, blue), PA_N (chain B, green), LF_N (chain C, red) and calcium ions (gray spheres). Right, slices through a surface rendering of the two LF_N-binding subsites, with the C-terminal binding subsite at top and the α-clamp subsite at bottom. (**c**) Axial rendering of the biological unit—the $PA_8(LF_N)_4$ complex—colored as in **b**. The PA octamer is shown as a molecular surface, and LF_N's helices and strands are cylinders and planks, respectively. The structure is produced from chains A, B and C, using the *C4* symmetry axis, which is parallel to the *c* edge of the unit cell at (–½*a*, 0*b*). (**d**) LF_N α1-β1 binds the α-clamp subsite formed at the interface of two PA subunits, driving the assembly of dimeric and tetrameric PA intermediates[19], which in turn form PA_8 complexes.

flexibility contained in an unfolding substrate? These questions have remained unanswered, in part because atomic resolution structures of unfolding intermediates in complex with these clamps have not been described. Here we report a structure of a partially unfolded substrate, the PA-binding domain of LF, in complex with its unfolding machine, the PA oligomer.

RESULTS

Crystal structure of the $PA_8(LF_N)_4$ complex

For these crystallographic studies, we focused on the PA_8 oligomer, considering its enhanced thermostability as well as its advantageous fourfold, square-planar symmetry[19]. By MS, we found that the PA_8LF_4 complex is physiologically relevant, as it assembles from the full-length, wild-type (WT) PA and LF subunits (**Supplementary Fig. 2a**). Our best-diffracting crystals contain LF_N (LF residues 1–263) and a PA construct lacking its membrane-insertion loop[19], which is superfluous to the known PA-LF_N interaction[34]. LF_N, the minimal portion of LF that specifically binds PA[35], can translocate heterologous domains as N- or C-terminal fusions into cells[36,37]. EF contains a homologous PA-binding domain, and it is likely that the PA-LF_N interaction is general to LT and ET complexes[38]. Homogenous $PA_8(LF_N)_4$ complexes (**Supplementary Fig. 2b**) form crystals in the $P42_12$ space group that diffract X-rays to 3.1 Å (**Table 1**). Molecular replacement solutions identified two PA_2 complexes and significant (2.7σ) unassigned electron density ($F_o - F_c$) for α helices located proximal to the domain 1′ (D1′) surface of each PA_2 complex. Rounds of polyalanine-helix modeling and refinement revealed that the novel helical density aligns well with α2, α4, α9 and α10 of LF_N. The two occurrences of the PA_2LF_N ternary complex (**Fig. 1b**) in the asymmetric unit are structurally identical; its PA subunits are structurally similar to the full-length PA monomer[20] and the PA subunits observed in the PA_7 and PA_8 prechannel oligomers[19,24]. Thus the biological unit—the $PA_8(LF_N)_4$ prechannel complex (**Fig. 1c**)—comprises four PA_2LF_N ternary complexes (**Fig. 1d**).

Notably, LF_N α1-β1 (residues 29–50) unfolds and adopts a novel conformation relative to free LF (PDB 1J7N[23]). LF_N α1-β1 docks in the cleft formed between adjacent PA subunits and aligns well with the experimental electron density (**Fig. 2a**,**b**). We can assign this unique conformation of α1-β1 because it extends from LF_N α2 as a contiguous stretch of electron density contoured at σ = 1 (**Supplementary Fig. 3a**). LF_N's C terminus also reveals well-defined electron density (**Fig. 2c**). Overall, LF_N excludes 1,900 Å^2 of solvent-accessible surface area (SASA) on the PA dimer. This surface is composed of two discontinuous LF_N-binding subsites (**Fig. 1b**) formed by adjacent PA subunits, termed PA_N and PA_C (to reflect whether the PA subunit interacts primarily with the N or C terminus of LF_N, respectively). The details of these respective subsites, called the α-clamp binding subsite and the C-terminal binding subsite, are depicted in **Figure 3a**,**b**. Thus, upon binding the PA oligomer, LF_N partially unfolds, whereby its first α-helix and β-strand (i) separate from the main body of the protein, (ii) dock into the cleft between two adjacent PA subunits (**Fig. 1b**) and (iii) orient toward the center of the PA oligomer lumen (**Fig. 1c**).

Structures of the C-terminal and α-clamp–binding subsites

At the C-terminal subsite, LF_N's C-terminal subdomain excludes ~900 Å^2 on PA_C (**Fig. 3b**). The structure reveals a hydrophobic interface, involving PA_C Phe202, Pro205, Ile207 and Ile210 and

Table 1 Data collection and refinement statistics

	$PA_8(LF_N)_4$ [a]
Data collection	
Space group	$P42_12$
Cell dimensions	
a, *b*, *c* (Å)	178.38, 178.38, 240.36
Resolution (Å)	49.8–3.1 (3.2–3.1)[b]
$R_{p.i.m.}$[c]	6.9 (46.0)
$I / \sigma I$	11.4 (2.2)
Completeness (%)	92.0 (78.0)
Redundancy	7.9 (8.0)
Refinement	
Resolution (Å)	49.8–3.1
No. reflections	65,165
R_{work} / R_{free}	24.9 / 28.1
No. atoms	
Protein	20,397
Ligand/ion	8
Water	4
B-factors	
Protein	100.7
Ligand/ion	53.3
Water	56.7
R.m.s. deviations	
Bond lengths (Å)	0.005
Bond angles (°)	0.610

[a]Data for this complex were collected from a single crystal. [b]Values in parentheses are for the highest-resolution shell. [c]$R_{p.i.m.}$, precision-indicating *R* factor.

LF Val232, Leu235, His229, Tyr223, Leu188 and Tyr236. In particular, LF Tyr236 is well packed against PA_C Ile210 (**Fig. 2c**), and its phenol hydroxyl forms a hydrogen-bonding network with PA_C His211 and Asp195 near the center of the hydrophobic interface (**Fig. 3b**). Additional electrostatic interactions surround this hydrophobic core. The side chain of PA_C Glu190 forms a pair of hydrogen bonds with both the γ-hydroxyl and amide nitrogen of LF Thr141; PA_C Lys197, Lys213, Lys214 and Lys218 form salt bridges with LF Asp182, Asp187, Asp184 and Glu142, respectively; and PA_N Arg200 forms a salt bridge with LF Glu139. PA and LF residues localized in this binding subsite are corroborated by mutagenesis studies, probing binding (**Fig. 3c**,**d**), assembly and binding (**Supplementary Fig. 4a**)[34,38–41] and cytotoxicity[41] (**Supplementary Fig. 4b**,**c**).

At the α-clamp subsite, PA_N and PA_C interact with LF_N's unfolded α1 and β1 structures (**Fig. 3a**). Remarkably, hydrogen bonds lost upon LF_N unfolding are reformed on the surface of PA: LF_N α1 maintains a similar helical conformation, and LF_N β1 (Ile43 and Lys45) forms parallel β-sheet hydrogen bonds with Leu203 in PA_N β13 (**Fig. 2b**). PA_N Pro205, which is positioned at the end of PA_N β13, terminates the parallel-sheet interactions with LF_N β1. Overall, LF_N α1-β1 excludes 1,000 Å^2 of SASA on PA. LF_N α1 is docked deep into the α-clamp cleft at the interface of adjacent PA subunits (**Figs. 1b** and **3a**). Reminiscent of what is seen in calmodulin complexes with peptide helices[42,43], PA's twin Ca^{2+}-binding sites scaffold the cleft and define its distinct shape and chemical character, including (i) a delocalized anionic potential created by the excess of negatively charged PA residues chelating the two Ca^{2+} ions and (ii) a large proportion of SASA contributed by PA backbone atoms. LF_N's side chains are not well packed with side chains in the α-clamp cleft, in contrast to the C-terminal binding subsite (**Fig. 3a**,**b**). Notably, PA contacts the side chains of LF Met40 and His35 through backbone interactions. PA_C Arg178 contacts the hydrophilic face of α1 at LF His42 while maintaining a hydrogen bond with the backbone carbonyl of PA_N Thr201. Aromatic residues, PA_N Phe236 and Phe464, and aliphatic residues, PA_N Leu187 and Leu203, line the cleft face opposite of PA_C Arg178. Upon binding LF_N, PA_N Phe202 repositions its phenyl group toward LF_N β1, shielding β1's backbone hydrogen bonds with PA_N Leu203. The chemical nature of the α-clamp cleft suggests that it is well suited to bind an unfolded β-strand and an amphipathic helix with a positively charged face.

Both LF-binding subsites are critical for cytotoxicity activity

We initially characterized the PA-LF binding interaction using cytotoxicity assays. Site-directed mutagenesis studies of PA and LF residues involved in either binding subsite revealed defects in LT-induced macrophage cytolysis (**Supplementary Fig. 4b**,**c**). To further address the interaction between LF_N's α1-β1 sequence and the α clamp, we created fusions of the first 20 or 60 residues of LF with the A fragment from diphtheria toxin (DTA), called $LF_{1–20}$-DTA and $LF_{1–60}$-DTA, respectively. When administered with PA, we found that $LF_{1–60}$-DTA was 100-fold more cytotoxic than $LF_{1–20}$-DTA or hexahistadine-tagged DTA (His_6-DTA, DTA with an N-terminal, 18-residue leader containing the hexahistidine sequence; **Supplementary Fig. 4d**). Notably, despite lacking the α1–β1 sequence, His_6-DTA[44] and $LF_{1–20}$-DTA were cytotoxic when administered in combination with WT PA (**Supplementary Fig. 4d**); however, all of these DTA constructs were much less cytotoxic, by a factor of ~1,000, when administered with the α-clamp mutant PA R178A (**Supplementary Fig. 4e**). The α clamp thus has broad substrate specificity. However, the role of the interaction of α1-β1 and the α-clamp in toxin function is difficult to deduce from cytotoxicity assays alone because toxin uptake involves multiple steps (for example, PA assembly, LF binding, unfolding and translocation).

The role of the α clamp in LT assembly

To determine the role of the α clamp in LT assembly, we performed multiple *in vitro* PA-LF_N assembly assays. By native PAGE, we found that PA mutations introduced into the LF_N-PA–binding interface

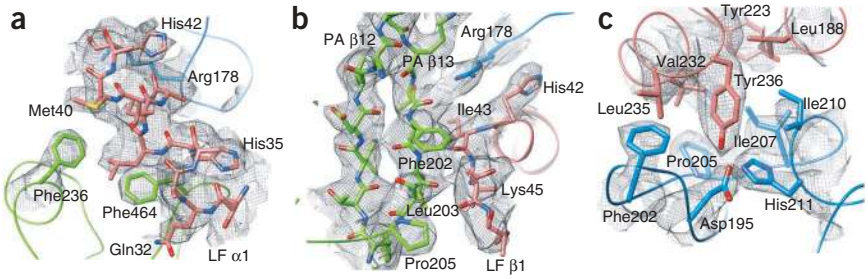

Figure 2 LF_N electron density in the $PA_8(LF_N)_4$ complex. A composite simulated-annealing (SA) omit map calculated in PHENIX[51] to 3.1 Å contoured at $\sigma = 1$ (gray mesh). The models of PA_N, PA_C and LF_N are rendered in green, blue and red, respectively. Secondary structure elements and individual residues are labeled. Nitrogen, oxygen and sulfur atoms are colored blue, red and yellow, respectively. (**a**) LF_N α1 (residues 31–42) in complex with PA_N. Lysine and glutamate residues are truncated to Cβ for clarity. (**b**) LF_N β1 in complex with PA_N β12-β13. LF_N Lys45 is truncated to Cβ for clarity. (**c**) LF_N's C-terminal binding subsite interaction with PA_C. Additional stereo-pair images of LF_N omit maps following SA refinement are depicted in **Supplementary Figure 3**.

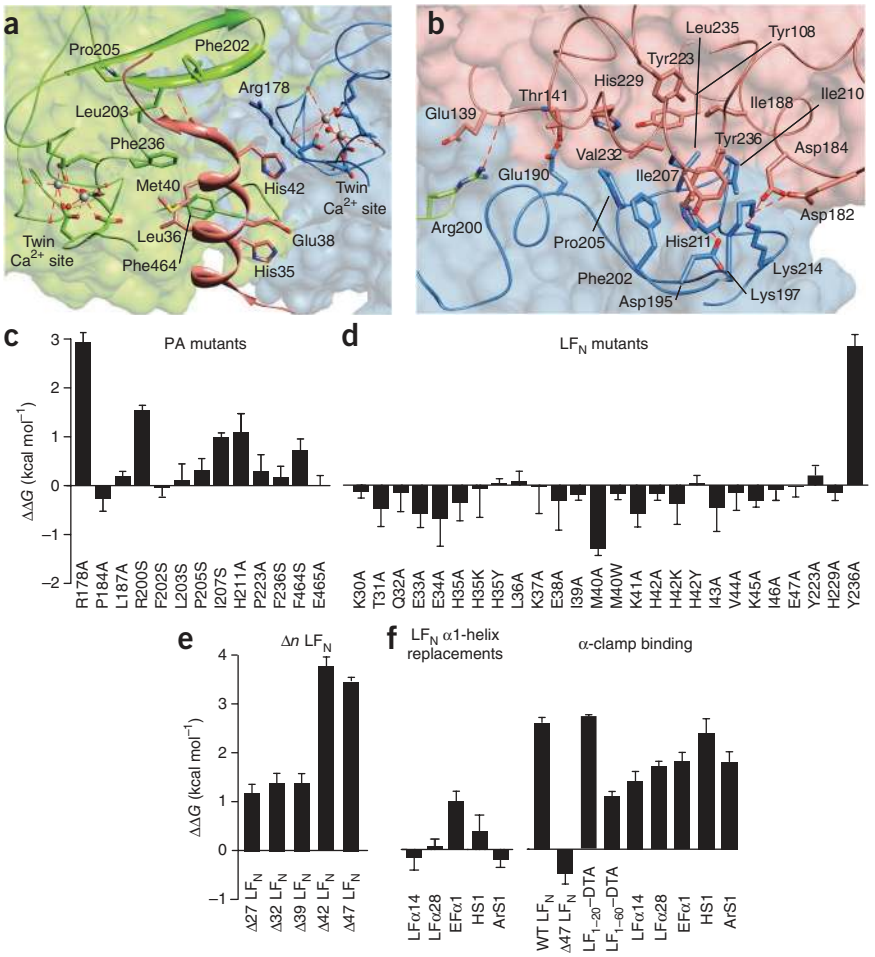

Figure 3 The PA octamer binds LF_N in two distinct subsites. (**a**,**b**) Detailed views of the α-clamp binding subsite (**a**) and the C-terminal binding subsite (**b**). Highlighted noncovalent interactions are indicated with red dashed lines. Chains and Ca^{2+} ions are colored as in **Figure 1b**. (**c**–**e**) Changes in equilibrium binding free energy ($\Delta\Delta G$) for PA channel complexes, comparing site-directed mutants of PA (**c**), site-directed mutants of LF_N (**d**) and Δn LF_N N-terminal truncation mutants (**e**). In **c**–**e**, the reference state is WT LF_N:WT PA. (**f**) Left, LF_N α1-β1 replacement mutant binding to WT PA; $\Delta\Delta G$ values are referenced to WT LF_N. Right, $LF_{1–20}$-DTA, $LF_{1–60}$-DTA, Δ47 LF_N and LF_N α1-β1 replacement mutant binding to PA R178A; $\Delta\Delta G$ values are referenced to WT PA. LF_N α1-β1 replacement mutants include either multiple point mutations in the α1-β1 sequence (^{32}QEEHLKEIMKHIVK^{46}I) or replacements of the α1-β1 sequence with other sequences from LF or EF. The replacement sequence and sequence identity (%) for each are as follows: LFα14, SEEGRGLLKKLQI (23%); LFα28, NSKKFIDIFKEEG (23%); EFα1, EKEKFKDSINNLV (31%); hydrophilic sequence 1 (HS1), QEEHSKEISKHSVKS (73%); aromatic sequence 1 (ArS1), QEEHFKEIFKHFVKF (73%). See **Supplementary Figure 7** for alignments and helical-wheel depictions of the α1-β1 replacement sequences. In **c**–**f**, $\Delta\Delta G = RT \ln K_d^{MUT}/K_d^{WT}$, where the equilibrium dissociation constants (K_d) were measured for the mutant (MUT) and WT proteins at pH 7.4, $\Delta\psi = 0$ mV (**Supplementary Fig. 6**); R is the gas constant; and T is the temperature. Values are given as mean ± s.d. (n = 2–6).

disrupted assembly of PA with LF_N (**Supplementary Fig. 4a**). To focus on the role of LF_N α1-β1 in PA assembly, we labeled PA K563C with two different fluorescent probes. A 1:1 ratiometric mixture of these labeled $_n$PA K563C constructs ($_n$PA*) produces an increase in fluorescence resonance energy transfer (FRET) upon assembly with LF_N[45]. Using this FRET assay, we found that fivefold more $_n$PA* assembled with WT LF_N than with the Δ47 LF_N N-terminal truncation (which lacks both α1 and β1; **Supplementary Fig. 5a**). The circular dichroism (CD) spectra of Δ47 and WT LF_N were comparable, demonstrating that the assembly defect is not due to the misfolding of Δ47 LF_N (**Supplementary Fig. 5b**). Using electron microscopy (EM), native PAGE and MS, we found that the percentage of octameric PA oligomers was greatly reduced for Δ47 LF_N relative to WT LF_N (**Supplementary Fig. 5c**–**e**). By EM, we estimated that ~3% of the PA oligomers produced with Δ47 LF_N were octameric (one-tenth as much as observed with WT LF_N; **Supplementary Fig. 5d**). Thus not only do LF_N's α1 and β1 structures drive PA oligomerization, but they are also critical to the mechanism of PA octamer formation (**Fig. 1d**).

Mapping the LF_N-binding interaction with the PA channel

Using electrophysiology, we measured LF_N binding by observing kinetic and equilibrium changes in channel conductance[8] (**Supplementary Fig. 6a**–**c**); these result from the fact that when LF_N binds to the PA channel, it inserts its N-terminal end into the channel and blocks conductance. We monitored binding in the absence of an applied $\Delta\psi$ to eliminate its influence on the channel-substrate interaction. Because PA_7 and PA_8 have similar translocation[19] and cell cytotoxicity[22] activities, we used the PA_7 oligomer to maintain consistency with prior reports[7–9]. To determine the overall thermodynamic contribution of LF_N α1-β1, we made a series of additional Δn LF_N N-terminal truncations (where n is the number of deleted residues). These Δn LF_N do not block PA channel conductance, as they lack sufficient unfolded and unstructured sequence on their N termini. We used a competition assay to measure Δn LF_N binding: first we blocked PA channel conductance with WT LF_N (~100 pM); then we added the competitor Δn LF_N and monitored the restoration of the conductance (**Supplementary Fig. 6d**,**e**). We found that Δ42 and Δ47 LF_N reduced WT PA channel–binding affinity by 3.6–3.8 kcal mol^{-1} relative to WT LF_N (**Fig. 3e**). However, because Δ27, Δ32 and Δ39 LF_N destabilize the complex by about 1.2–1.4 kcal mol^{-1}, the α1-β1 interaction provides ~2.5 kcal mol^{-1} of stabilization. We assume that downstream interactions within the channel provide the additional ~1 kcal mol^{-1} of stabilization. We conclude that LF_N α1-β1 binds to the PA channel and provides substantial stabilization of the PA-LF_N complex.

To investigate the details of the interaction between the PA channel and LF_N, we engineered point mutations into residues localized in either LF_N binding subsite and estimated their relative energetic contribution to channel binding (**Fig. 3c**,**d**). Several mutations localized in the C-terminal binding subsite, PA R200S, I207S and H211A, disrupted LF_N binding by 1–1.5 kcal mol^{-1}. These residues form two binding 'hot spots'—that is, locations where point mutations disrupt binding most severely[46]. By contrast, the mutations F202S and P205S, located between these two C-terminal–site hot spots, had minimal effects on LF_N binding, reflecting the fact that LF_N's C terminus does

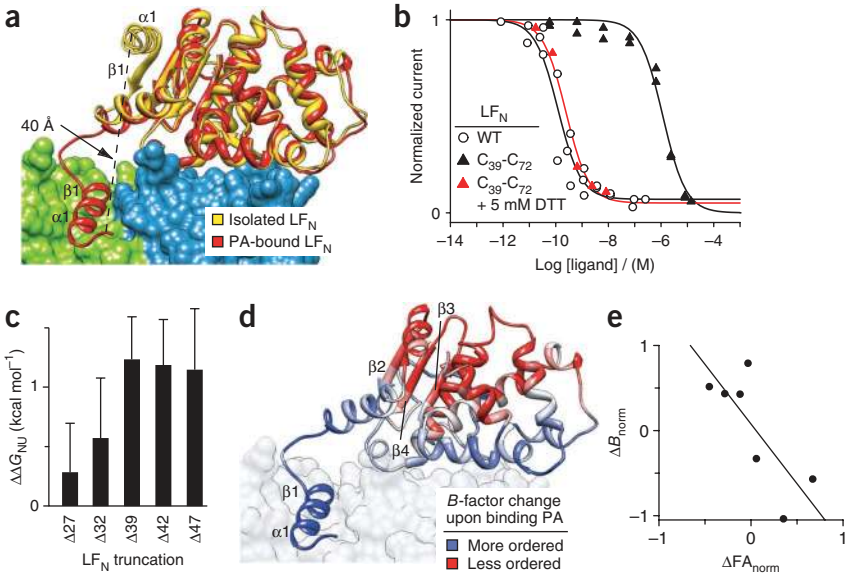

Figure 4 Dynamics and thermodynamics of the pre-translocation unfolding of LF_N. (**a**) Rendering of LF_N's unfolding transition on the surface of the PA_NPA_C dimer (green and blue, respectively). Free LF_N (gold) (PDB 1J7N[23]) is Cα-aligned to the LF_N in the $PA_8(LF_N)_4$ complex (red). (**b**) $LF_N^{C39\text{-}C72}$ binding to WT PA channels (pH 7.4, 0 mV) in the presence of 5 mM DTT (red triangles) and in the absence of DTT (black triangles). A WT LF_N binding curve (open circles) is also shown. Normalized equilibrium currents were fit to a single-site binding model to obtain K_d values: WT LF_N, K_d = 120 (±30) pM; $LF_N^{C39\text{-}C72}$, K_d = 1.2 (±0.1) μM; and $LF_N^{C39\text{-}C72}$ + 5 mM DTT, K_d = 240 (±60) pM. (**c**) Equilibrium stability measurements (pH 7.5, 20 °C) of N-terminal truncations of LF_N (Δ*n* LF_N). Equilibrium free energy differences ($\Delta\Delta G_{NU}$) were obtained from denaturant titration data fit to a four-state equilibrium unfolding model[26] (**Supplementary Fig. 9b**), where $\Delta\Delta G_{NU} = \Delta G_{NU}(\Delta n) - \Delta G_{NU}(WT)$. Values are given as mean ± s.d. (n = 3 or 4). Fit parameters are listed in **Supplementary Table 1**. (**d**) Residues in LF_N colored by their differences in normalized *B*-factor (ΔB_{norm}), which is obtained by comparing the model of free LF_N (PDB 1J7N, structure 1) and LF_N in complex with PA (structure 2) using $\Delta B_{norm} = B_{1,i} / \langle B_1 \rangle - B_{2,i} / \langle B_2 \rangle$, where $\langle B \rangle$ is the average *B*-factor for the entire chain. (**e**) ΔB_{norm} is plotted against the normalized fluorescence anisotropy (FA) change (ΔFA_{norm}) for seven different site-specifically labeled residues (37, 48, 72, 126, 164, 199 and 242) in LF_N. $\Delta FA_{norm} = FA_{1,i} / \langle FA_1 \rangle - FA_{2,i} / \langle FA_2 \rangle$, where free LF_N and the LF_N-PA oligomer complex are state 1 and state 2, respectively. The linear fit is significant (P = 0.04). Raw anisotropy changes upon binding the PA oligomer for these labeled LF_N are shown in **Supplementary Figure 10**.

not make substantial contact with these residues (**Fig. 3b**). The LF_N Y236A mutant most appreciably perturbed PA-channel binding and represents the LF_N hot spot in the C-terminal subsite interaction. Other adjacent LF_N residues in the C-terminal subsite interaction had minimal effects on PA channel binding.

We then investigated the relative energetic contribution of residues localized in the α-clamp binding subsite (**Fig. 3c**,**d**). We found that PA Arg178 comprises the major hot-spot site in PA's α clamp, where the R178A mutation destabilized the complex by 2.9 kcal mol^{-1}. Although the aromatic PA mutant F464S destabilized LF_N binding at the α-clamp site by 0.7 kcal mol^{-1}, the PA F236S mutant did not. Additionally, we found that none of 23 point mutations introduced into LF_N α1 and β1 destabilized the LF_N-PA channel complex. Notably, the mutation LF_N M40A stabilized the complex by 1.3 kcal mol^{-1} (**Fig. 3d**). These results indicate that the two different LF_N-binding subsites have contrasting binding-energetic behaviors. At the C-terminal subsite, a classical interface is observed in which specific LF_N and PA side chains comprise the respective hot spots on either interface. At the α-clamp subsite, although we identified PA Arg178 as a major hot-spot residue, no clear hot spot could be identified on LF_N α1-β1. These observations suggest that the stabilizing interactions in the α-clamp subsite do not involve specific LF_N side chains and that the ~2.5 kcal mol^{-1} of binding stabilization is instead due to the formation of nonspecific contacts and the more general exclusion of SASA.

The PA α clamp possesses nonspecific binding activity

The robustness of the binding interaction is intriguing given the paucity of specific α-clamp interactions. To test the specificity of the α-clamp interaction, we either replaced the entire LF_N α1-β1 sequence with other nonhomologous sequences from LF and EF or introduced multiple mutations into α1-β1 (**Supplementary Fig. 7**). Notably, we found that these LF_N α1-β1 replacements bound with affinities similar to those of WT LF_N (differing by 0.2–1.0 kcal mol^{-1}; **Fig. 3f**). Furthermore, multisite LF_N mutants in which the buried hydrophobic face of α1-β1 was replaced with either four serine residues (LF_N HS1) or four phenylalanine residues (LF_N Ar1) bound PA with similar affinity as WT LF_N (**Fig. 3f**), indicating that the α clamp also binds nonamphipathic helices. Finally, we found that these LF_N α1-β1 replacement constructs bound 1.3–2.4 kcal mol^{-1} less tightly to PA R178A relative to WT PA (**Fig. 3f**), thereby confirming that this nonspecific binding activity is localized to the α-clamp subsite. Thus the α clamp binds a broad array of sequences, providing 1.5–4 kcal mol^{-1} of stabilization (depending upon the identity of the α1-β1 sequence).

LF_N must unfold to bind the α-clamp subsite

Our crystal structure and thermodynamic binding data indicate that the α-clamp subsite binds nonspecifically to unfolded protein substrates. This model is well supported by several additional lines of evidence. First, the thermodynamic comparison of WT LF_N and the truncated Δ*n* LF_N mutants is appropriate because these mutants had similar folded secondary structure content to WT LF_N (**Supplementary Fig. 5b**). Moreover, the Δ47 LF_N construct bound similarly to PA R178A as to WT PA (**Fig. 3f**), confirming that the Δ47 LF_N truncation does not bind at the α-clamp site, as implied by the structure (**Fig. 1b**). Second, fusions of LF's N terminus and DTA (LF_{1-60}-DTA and LF_{1-20}-DTA) were sufficient to bind to the α-clamp site, as their affinity for the PA channel is disrupted by the PA R178A mutation (**Fig. 3f** and **Supplementary Fig. 8**). This result indicates that the α clamp is an independent binding site capable of binding to unstructured sequences at the N terminus of a substrate. Third, knowing that LF_N α1-β1 unfolds upon binding PA (**Fig. 4a**), we engineered the double mutant LF_N I39C E72C ($LF_N^{C39\text{-}C72}$), which forms a disulfide bond that prevents α1-β1 unfolding. Notably, under nonreducing conditions, $LF_N^{C39\text{-}C72}$ had an affinity for PA channels

that is reduced by a factor of 10^4 from that of WT LF_N (**Fig. 4b**); however, under reducing conditions (in the presence of dithiothreitol, DTT), $LF_N^{C39\text{-}C72}$ bound with the same affinity as WT LF_N (**Fig. 4b**). Kinetic data also revealed a DTT-dependent $LF_N^{C39\text{-}C72}$ blockade of PA channels (**Supplementary Fig. 9a**). Therefore, LF_N must unfold α1 and β1 to properly bind the α clamp and interact stably with PA oligomers.

We then asked how the unfolding of LF_N α1-β1 on the surface of PA affects the remaining folded structure of LF_N. First, we measured the stability of the Δ*n* LF_N mutants using chemical denaturant titrations probed by CD at 222 nm (CD_{222}). The Δ*n* mutants' stabilities were estimated by fitting the CD_{222}-probed titration data to a four-state equilibrium unfolding model ($N \rightleftarrows I \rightleftarrows J \rightleftarrows U$)[26] (**Supplementary Fig. 9b** and **Supplementary Table 1**). We found that the truncation mutants possess native (*N*), intermediate (*I* and *J*) and unfolded (*U*) states. The truncations, however, destabilized the *N* state by ~1.2 kcal mol^{-1}, with the deletion of the α1-helix being more destabilizing than the deletion of the β1-strand (**Fig. 4c**). Second, we compared the crystallographic atomic displacement parameters (*B*-factors) of bound LF_N with free LF_N (PDB 1J7N[23]). In this analysis, we calculated the relative change in normalized *B*-factor (ΔB_{norm}) for each LF_N residue upon binding PA (**Fig. 4d**). The β2-β4 sheet and surrounding helices show increased B_{norm} upon binding PA, whereas α1-β1 show decreases in B_{norm} (**Fig. 4d**). To corroborate these ΔB_{norm} values, we measure changes in backbone and side chain mobility using fluorescence anisotropy (FA). LF_N mutants with unique cysteine substitutions were labeled with thiol-reactive fluorescent probes. Upon binding WT PA_7 oligomers, the fluorescent probes attached to LF_N's α1-β1 structures showed gains in normalized relative FA (FA_{norm}), and conversely, probes in the β2-β4 sheet showed losses in FA_{norm} (**Supplementary Fig. 10a**). Overall, these ΔFA_{norm} values inversely correlated with ΔB_{norm} values ($P = 0.04$, **Fig. 4e**), confirming that the more dynamic regions in the crystal are also dynamic in solution. Therefore, we conclude that the ~2.5 kcal mol^{-1} of stabilization gained when α1-β1 binds to the α-clamp site not only offsets the ~1.2 kcal mol^{-1} of thermodynamic destabilization imparted by the unfolding of α1-β1 but also accounts for the observed entropic increases in strain and disorder throughout LF_N's remaining folded structure.

The role of the α clamp in protein translocation

To determine the role of the α clamp during protein translocation, we use planar lipid bilayer electrophysiology, which records changes in PA conductance as substrate-blocked channels translocate their substrates and reopen[7–9]. We examined 37 point mutations in PA and LF_N. Of the 13 PA mutants tested, we found that the α-clamp mutant, PA F202S, slowed LF_N translocation by a factor of 20, or 1.7 kcal mol^{-1} (**Fig. 5a**). A subset of the LF_N point mutations (H35A, M40A, and H42A), which point toward either face of the α-clamp cleft (**Fig. 3a**), inhibited translocation by 0.8–1.7 kcal mol^{-1} (**Fig. 5a**). These translocation defects were observed for both PA_7 and PA_8 channels (**Supplementary Fig. 11a**). Conversely, other buried α1 sites (LF_N Leu36, Ile39 and Ile43) were tolerant of substitution and did not affect protein translocation (**Fig. 5a**). Notably, we found that the observed positional translocation defects were restored when a

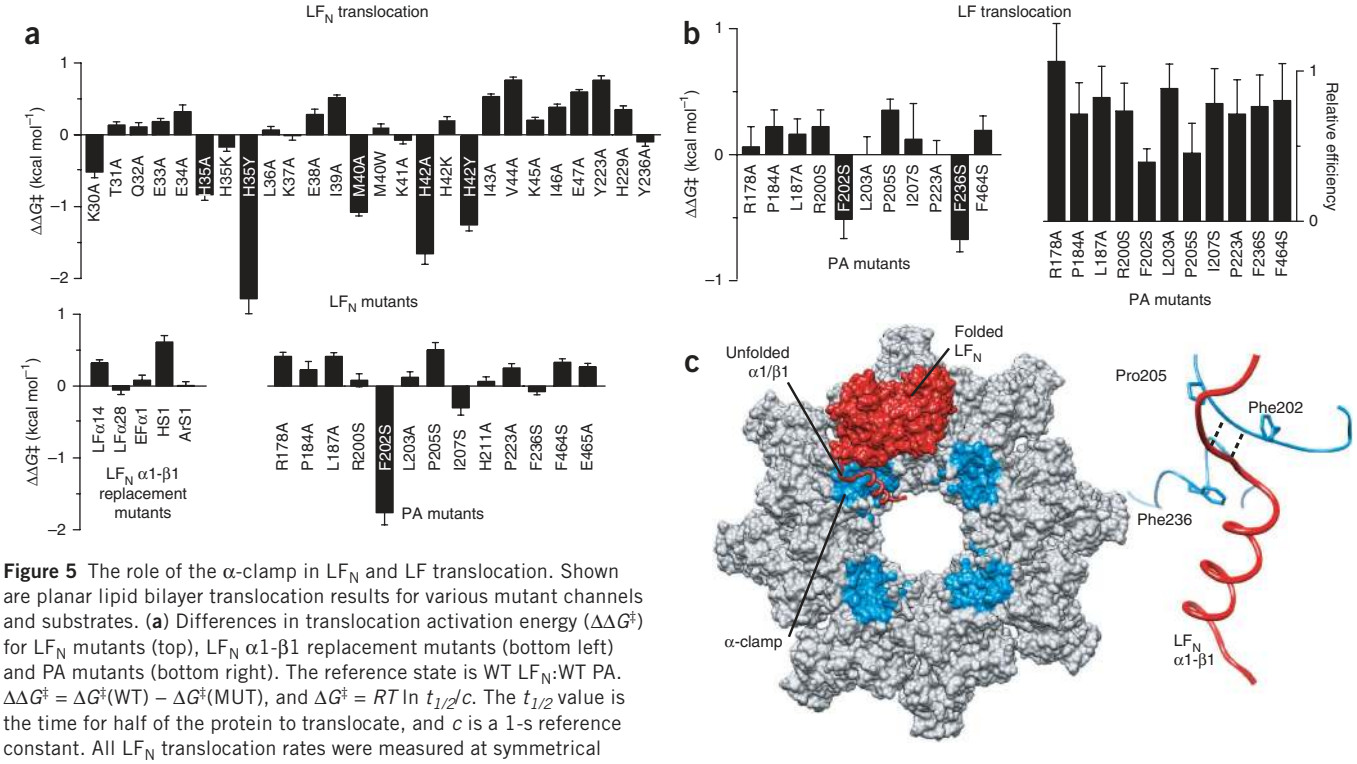

Figure 5 The role of the α-clamp in LF_N and LF translocation. Shown are planar lipid bilayer translocation results for various mutant channels and substrates. (**a**) Differences in translocation activation energy ($\Delta\Delta G^{\ddagger}$) for LF_N mutants (top), LF_N α1-β1 replacement mutants (bottom left) and PA mutants (bottom right). The reference state is WT LF_N:WT PA. $\Delta\Delta G^{\ddagger} = \Delta G^{\ddagger}(WT) - \Delta G^{\ddagger}(MUT)$, and $\Delta G^{\ddagger} = RT \ln t_{1/2}/c$. The $t_{1/2}$ value is the time for half of the protein to translocate, and *c* is a 1-s reference constant. All LF_N translocation rates were measured at symmetrical pH 5.6, $\Delta\psi = 40$ mV. A negative value indicates that the rate of translocation slowed upon mutation. The relative translocation efficiencies for these LF_N translocations are given in **Supplementary Figure 11b**. (**b**) Full-length LF translocation at $pH_{cis} = 6.1$, $pH_{trans} = 7.4$, $\Delta pH = 1.3$, $\Delta\psi = 20$ mV. Shown are $\Delta\Delta G^{\ddagger}$ values (left) and relative translocation efficiencies ($\varepsilon_{MUT}/\varepsilon_{WT}$) (right) for mutant PA channels. Individual LF translocation records are shown in **Supplementary Figure 12**. Values in **a**,**b** are given as mean ± s.d. ($n = 2$–12). (**c**) Left, LF_N α1-β1 (red ribbon) unfolds from the structured C-terminal subdomain (red surface) by binding into the α-clamp site (cyan surface) on the PA oligomer (gray surface). The interaction is composed of nonspecific interactions. The α-clamp sites orient the unfolded structure toward the central pore, where the protein is translocated. Right, residues in PA's α-clamp site (cyan) that affect LF_N and/or LF translocation are rendered as sticks. LF_N α1-β1 (red ribbon) and parallel β-sheet hydrogen bonds (black dotted lines) between LF_N β1 and PA β13 are shown.

bulky group was placed at position 40 (ref. 9) and positively charged residues were placed at positions 35 and 42 (**Fig. 5a**). All of the LF_N α1-β1 replacements translocated similarly to WT LF_N (**Fig. 5a**). We conclude, therefore, that efficient LF_N unfolding and translocation are catalyzed by the aromatic α-clamp residue (PA Phe202); however, the LF_N α1-β1 sequence itself has rather minimal charge and steric requirements.

The broad substrate specificity of the α clamp led us to ask which PA residues facilitate translocation of full-length LF, a more complex, multidomain substrate. LF has a different rate-limiting step than does LF_N and requires a greater driving force[7]; therefore, we measured its translocation kinetics under ΔpH and $\Delta\psi$. We found that the PA α-clamp mutants F202S and P205S reduced LF translocation efficiency, ε, by ~60% (where $\varepsilon = A_{obs}/A_{exp}$; A_{exp} and A_{obs} are the expected and observed amplitudes, respectively; **Supplementary Fig. 12**). The PA mutants F236S and F202S inhibited the rate of LF translocation (**Fig. 5b**). These PA mutants did not appreciably affect LF_N binding (**Fig. 3c**), however, and only PA F202S inhibited LF_N translocation (**Fig. 5a**). Finally, we found that PA R178A was defective in LF_N binding but not defective in translocation. We conclude that hydrophobic and aromatic residues surrounding the α clamp (**Fig. 5c**) catalyze the translocation of LF.

DISCUSSION

Some models[8,30] propose that nonspecific clamping sites are critical features of unfolding machines. In general, unfoldases are thought to denature proteins by applying mechanical forces[9] and transiently trapping partially unfolded conformations in nonspecific binding sites[8]. Unfolded protein, however, is inherently more complex than folded protein, especially in terms of its configurational flexibility and combinatorial chemical complexity. Therefore, a translocase channel would have to accommodate an ever-changing array of possible chemistries and configurations as the unfolded chain is translocated. An elegant solution to this problem may be that unfolded sequences adopt a more rigid and uniform α-helical or β-strand conformation upon binding to an unfoldase, as we observed in the PA-LF_N complex (**Fig. 3a**). Indeed, we found that PA's α clamp can bind to a broad array of amino acid sequences (**Fig. 3f**). This nonspecific binding activity likely reflects the general helical shape complementarity of the α-clamp site, which excludes ~1,000 $Å^2$ on PA without making specific side chain–side chain interactions. Additionally, backbone hydrogen bonds, which are ubiquitous features of polypeptides, can provide nonspecific contact points between the translocase and substrate, as we observed between LF_N β1 and PA_N β13 (**Figs. 3a** and **5c**).

Broad peptide-binding specificity has been observed in other systems, including calmodulin[42,43], the ClpXP adaptor SspB[32,33], the chaperone GroEL–GroES[47–49] and the unfoldase ClpA/Hsp100 (ref. 31). For calmodulin, which is analogous structurally to the PA oligomer's α-clamp cleft, multiple peptide helices are recognized by the cleft formed by its twin Ca^{2+}-ion binding sites. The ClpXP adaptor SspB binds multiple unstructured C-terminal degradation signal tags in various conformations in a cleft. The chaperone complex GroEL–GroES can bind to various amphipathic helices and strands. A substrate binding site identified in the unfolding machine ClpA/Hsp100 is located above the ϕ-clamp–type site and may be analogous to the α-clamp site on the PA oligomer.

Our structure provides new insight into how a nonspecific polypeptide clamp can unfold its substrate. Through binding to LF_N in multiple locations using nonspecific interactions (that is, in the α clamp (**Fig. 3a**) and ϕ clamp[8]), LF_N can be partially unfolded (**Fig. 4a**) and maintained in a more strained (**Fig. 4d**,**e**) and less stable conformation (**Fig. 4c**–**e**). The region of LF_N that is most destabilized upon binding PA (**Fig. 4d**,**e**) coincides with LF_N's β2-β4 sheet, which was previously reported as the mechanical breakpoint, or structure that is rate-limiting to the unfolding step of translocation[9]. Therefore, we infer that the α-clamp site stabilizes unfolding intermediates, introduces strain into the mechanical breakpoint and feeds unfolded structure into the central ϕ-clamp site.

We estimate that the costs associated with binding to the α-clamp site (**Fig. 3c**–**e**) may be offset by orienting the substrate toward the central lumen (**Fig. 5c**), thereby reducing the stability of the substrate (**Fig. 4c**) and minimizing the diffusional mobility of unstructured regions before (**Fig. 4d**,**e**) or during translocation[8]. We expect that nonspecific clamping sites should lessen the counterproductive diffusive motions expected for large sections of unfolded polypeptide chain by maintaining contact with the unfolded chain and further reducing backbone conformational entropy, thus allowing the $\Delta\psi$/ΔpH driving force to efficiently unfold[9] and translocate proteins[7] (**Fig. 5a**,**b**). Although the α clamp forms a stable complex with unfolded structure, this intermediate does not represent a thermodynamic trap. Rather, populating partially unfolded translocation intermediates would lower a much greater overall rate-limiting barrier expected in the absence of such intermediates, thereby allowing translocation to proceed on a biologically reasonable timescale.

METHODS

Methods and any associated references are available in the online version of the paper at http://www.nature.com/nsmb/.

Accession codes. Protein Data Bank: The structure factors and coordinates for the $PA_8(LF_N)_4$ complex have been deposited with accession code 3KWV.

Note: Supplementary information is available on the Nature Structural & Molecular Biology website.

ACKNOWLEDGMENTS

We thank H. Gong, E. Haddadian, T. Sosnick and K. Freed for assistance in refining the backbone torsional angles using their unpublished TOP algorithm; J. Colby for assistance in purifying constructs; M. Brown for constructing the pET15-LF_N-SalI vector; J. Berger and N. Echols for advice on crystallography; R. Zalpuri at the Robert D. Ogg Electron Microscope Laboratory; J. Holton and G. Meigs at the 8.3.1 beamline of the Advanced Light Source; and T. Sosnick, J. Collier, J. Berger and J. Kuriyan for helpful advice. This work was supported by University of California start-up funds (B.A.K.) and US National Institutes of Health research grants R01-AI077703 (B.A.K.) and R01-GM064712 (E.R.W.).

AUTHOR CONTRIBUTIONS

G.K.F. crystallized, solved and refined the $PA_8(LF_N)_4$ structure. G.K.F., K.L.T., H.J.S., A.F.K., S.G.G. and I.I.T. obtained functional data. G.K.F., K.L.T., H.J.S., A.F.K., E.R.W. and B.A.K. prepared the manuscript.

COMPETING FINANCIAL INTERESTS

The authors declare no competing financial interests.

Published online at http://www.nature.com/nsmb/.
Reprints and permissions information is available online at http://npg.nature.com/reprintsandpermissions/.

1. Wickner, W. & Schekman, R. Protein translocation across biological membranes. *Science* **310**, 1452–1456 (2005).
2. Navon, A. & Ciechanover, A. The 26 S proteasome: from basic mechanisms to drug targeting. *J. Biol. Chem.* **284**, 33713–33718 (2009).
3. Sauer, R.T. *et al.* Sculpting the proteome with AAA+ proteases and disassembly machines. *Cell* **119**, 9–18 (2004).
4. Cheng, Y. Toward an atomic model of the 26S proteasome. *Curr. Opin. Struct. Biol.* **19**, 203–208 (2009).

5. Young, J.A. & Collier, R.J. Anthrax toxin: receptor binding, internalization, pore formation, and translocation. *Annu. Rev. Biochem.* **76**, 243–265 (2007).
6. Matouschek, A. Protein unfolding—an important process in vivo? *Curr. Opin. Struct. Biol.* **13**, 98–109 (2003).
7. Krantz, B.A., Finkelstein, A. & Collier, R.J. Protein translocation through the anthrax toxin transmembrane pore is driven by a proton gradient. *J. Mol. Biol.* **355**, 968–979 (2006).
8. Krantz, B.A. *et al.* A phenylalanine clamp catalyzes protein translocation through the anthrax toxin pore. *Science* **309**, 777–781 (2005).
9. Thoren, K.L., Worden, E.J., Yassif, J.M. & Krantz, B.A. Lethal factor unfolding is the most force-dependent step of anthrax toxin translocation. *Proc. Natl. Acad. Sci. USA* **106**, 21555–21560 (2009).
10. Kenniston, J.A., Baker, T.A., Fernandez, J.M. & Sauer, R.T. Linkage between ATP consumption and mechanical unfolding during the protein processing reactions of an AAA+ degradation machine. *Cell* **114**, 511–520 (2003).
11. Martin, A., Baker, T.A. & Sauer, R.T. Pore loops of the AAA+ ClpX machine grip substrates to drive translocation and unfolding. *Nat. Struct. Mol. Biol.* **15**, 1147–1151 (2008).
12. Huang, S., Ratliff, K.S. & Matouschek, A. Protein unfolding by the mitochondrial membrane potential. *Nat. Struct. Biol.* **9**, 301–307 (2002).
13. Huang, S., Ratliff, K.S., Schwartz, M.P., Spenner, J.M. & Matouschek, A. Mitochondria unfold precursor proteins by unraveling them from their N-termini. *Nat. Struct. Biol.* **6**, 1132–1138 (1999).
14. Smith, H. & Keppie, J. Observations on experimental anthrax: demonstration of a specific lethal factor produced *in vivo* by *Bacillus anthracis*. *Nature* **173**, 869–870 (1954).
15. Friedlander, A.M. Macrophages are sensitive to anthrax lethal toxin through an acid-dependent process. *J. Biol. Chem.* **261**, 7123–7126 (1986).
16. Agrawal, A. & Pulendran, B. Anthrax lethal toxin: a weapon of multisystem destruction. *Cell. Mol. Life Sci.* **61**, 2859–2865 (2004).
17. Ezzell, J.W. & Abshire, T.G. Serum protease cleavage of *Bacillus anthracis* protective antigen. *J. Gen. Microbiol.* **138**, 543–549 (1992).
18. Milne, J.C., Furlong, D., Hanna, P.C., Wall, J.S. & Collier, R.J. Anthrax protective antigen forms oligomers during intoxication of mammalian cells. *J. Biol. Chem.* **269**, 20607–20612 (1994).
19. Kintzer, A.F. *et al.* The protective antigen component of anthrax toxin forms functional octameric complexes. *J. Mol. Biol.* **392**, 614–629 (2009).
20. Petosa, C., Collier, R.J., Klimpel, K.R., Leppla, S.H. & Liddington, R.C. Crystal structure of the anthrax toxin protective antigen. *Nature* **385**, 833–838 (1997).
21. Katayama, H. *et al.* GroEL as a molecular scaffold for structural analysis of the anthrax toxin pore. *Nat. Struct. Mol. Biol.* **15**, 754–760 (2008).
22. Kintzer, A.F. *et al.* Role of the protective antigen octamer in the molecular mechanism of anthrax lethal toxin stabilization in plasma. *J. Mol. Biol.* **399**, 741–758 (2010).
23. Pannifer, A.D. *et al.* Crystal structure of the anthrax lethal factor. *Nature* **414**, 229–233 (2001).
24. Lacy, D.B., Wigelsworth, D.J., Melnyk, R.A., Harrison, S.C. & Collier, R.J. Structure of heptameric protective antigen bound to an anthrax toxin receptor: a role for receptor in pH-dependent pore formation. *Proc. Natl. Acad. Sci. USA* **101**, 13147–13151 (2004).
25. Benson, E.L., Huynh, P.D., Finkelstein, A. & Collier, R.J. Identification of residues lining the anthrax protective antigen channel. *Biochemistry* **37**, 3941–3948 (1998).
26. Krantz, B.A., Trivedi, A.D., Cunningham, K., Christensen, K.A. & Collier, R.J. Acid-induced unfolding of the amino-terminal domains of the lethal and edema factors of anthrax toxin. *J. Mol. Biol.* **344**, 739–756 (2004).
27. Van den Berg, B. *et al.* X-ray structure of a protein-conducting channel. *Nature* **427**, 36–44 (2004).
28. Lum, R., Niggemann, M. & Glover, J.R. Peptide and protein binding in the axial channel of Hsp104. Insights into the mechanism of protein unfolding. *J. Biol. Chem.* **283**, 30139–30150 (2008).
29. Wang, J. *et al.* Crystal structures of the HslVU peptidase-ATPase complex reveal an ATP-dependent proteolysis mechanism. *Structure* **9**, 177–184 (2001).
30. Zimmer, J., Nam, Y. & Rapoport, T.A. Structure of a complex of the ATPase SecA and the protein-translocation channel. *Nature* **455**, 936–943 (2008).
31. Hinnerwisch, J., Fenton, W.A., Furtak, K.J., Farr, G.W. & Horwich, A.L. Loops in the central channel of ClpA chaperone mediate protein binding, unfolding, and translocation. *Cell* **121**, 1029–1041 (2005).
32. Levchenko, I., Grant, R.A., Flynn, J.M., Sauer, R.T. & Baker, T.A. Versatile modes of peptide recognition by the AAA+ adaptor protein SspB. *Nat. Struct. Mol. Biol.* **12**, 520–525 (2005).
33. Levchenko, I., Grant, R.A., Wah, D.A., Sauer, R.T. & Baker, T.A. Structure of a delivery protein for an AAA+ protease in complex with a peptide degradation tag. *Mol. Cell* **12**, 365–372 (2003).
34. Cunningham, K., Lacy, D.B., Mogridge, J. & Collier, R.J. Mapping the lethal factor and edema factor binding sites on oligomeric anthrax protective antigen. *Proc. Natl. Acad. Sci. USA* **99**, 7049–7053 (2002).
35. Arora, N. & Leppla, S.H. Residues 1–254 of anthrax toxin lethal factor are sufficient to cause cellular uptake of fused polypeptides. *J. Biol. Chem.* **268**, 3334–3341 (1993).
36. Arora, N. & Leppla, S.H. Fusions of anthrax toxin lethal factor with shiga toxin and diphtheria toxin enzymatic domains are toxic to mammalian cells. *Infect. Immun.* **62**, 4955–4961 (1994).
37. Milne, J.C., Blanke, S.R., Hanna, P.C. & Collier, R.J. Protective antigen-binding domain of anthrax lethal factor mediates translocation of a heterologous protein fused to its amino- or carboxy-terminus. *Mol. Microbiol.* **15**, 661–666 (1995).
38. Lacy, D.B., Mourez, M., Fouassier, A. & Collier, R.J. Mapping the anthrax protective antigen binding site on the lethal and edema factors. *J. Biol. Chem.* **277**, 3006–3010 (2002).
39. Lacy, D.B. *et al.* A model of anthrax toxin lethal factor bound to protective antigen. *Proc. Natl. Acad. Sci. USA* **102**, 16409–16414 (2005).
40. Melnyk, R.A. *et al.* Structural determinants for the binding of anthrax lethal factor to oligomeric protective antigen. *J. Biol. Chem.* **281**, 1630–1635 (2006).
41. Chauhan, V. & Bhatnagar, R. Identification of amino acid residues of anthrax protective antigen involved in binding with lethal factor. *Infect. Immun.* **70**, 4477–4484 (2002).
42. Meador, W.E., Means, A.R. & Quiocho, F.A. Target enzyme recognition by calmodulin: 2.4 A structure of a calmodulin-peptide complex. *Science* **257**, 1251–1255 (1992).
43. Meador, W.E., Means, A.R. & Quiocho, F.A. Modulation of calmodulin plasticity in molecular recognition on the basis of x-ray structures. *Science* **262**, 1718–1721 (1993).
44. Blanke, S.R., Milne, J.C., Benson, E.L. & Collier, R.J. Fused polycationic peptide mediates delivery of diphtheria toxin A chain to the cytosol in the presence of anthrax protective antigen. *Proc. Natl. Acad. Sci. USA* **93**, 8437–8442 (1996).
45. Christensen, K.A., Krantz, B.A. & Collier, R.J. Assembly and disassembly kinetics of anthrax toxin complexes. *Biochemistry* **45**, 2380–2386 (2006).
46. Clackson, T. & Wells, J.A. A hot spot of binding energy in a hormone-receptor interface. *Science* **267**, 383–386 (1995).
47. Landry, S.J. & Gierasch, L.M. The chaperonin GroEL binds a polypeptide in an alpha-helical conformation. *Biochemistry* **30**, 7359–7362 (1991).
48. Li, Y., Gao, X. & Chen, L. GroEL recognizes an amphipathic helix and binds to the hydrophobic side. *J. Biol. Chem.* **284**, 4324–4331 (2009).
49. Wang, Z., Feng, H., Landry, S.J., Maxwell, J. & Gierasch, L.M. Basis of substrate binding by the chaperonin GroEL. *Biochemistry* **38**, 12537–12546 (1999).
50. Duesbery, N.S. *et al.* Proteolytic inactivation of MAP-kinase-kinase by anthrax lethal factor. *Science* **280**, 734–737 (1998).
51. Adams, P.D. *et al.* Recent developments in the PHENIX software for automated crystallographic structure determination. *J. Synchrotron Radiat.* **11**, 53–55 (2004).

ONLINE METHODS

Plasmids and proteins. Site-directed mutagenesis was performed using the commercial Quikchange procedure (Agilent Technologies). $LF_{1–20}$-DTA and $LF_{1–60}$-DTA were produced by introducing an in-frame SacI restriction site into the pET15b-DTA vector[44] before the DTA reading frame. The Δn LF_N constructs were made as described[38]. LF_N α1-β1 replacement constructs were made using a three-step gene-synthesis procedure described in the **Supplementary Methods**. WT PA and PA mutants, including the construct used in the crystallization experiments, $PA^{\Delta MIL}$ (in which the membrane insertion loop, residues 303–324, was deleted and replaced with a type II turn sequence[19]), were expressed and purified as described[8]. Heptameric and octameric PA oligomers were produced as described[19]. LF, LF_N, His_6-DTA and mutants thereof were expressed and purified as described[7]. The His_6 tags were removed from LF and LF_N constructs with bovine α-thrombin as described (**Supplementary Methods**). For fluorescence anisotropy studies, the cysteine-reactive fluorophore 5-((2-((iodoacetyl)amino)-ethyl)amino)naphthalene-1-sulfonic acid (IAEDANS) was used to label individual sites on cysteine-substituted LF_Ns (**Supplementary Methods**).

Crystallization, X-ray diffraction and model refinement. Soluble $PA^{\Delta MIL}$ octamer[19] (judged pure by EM) was complexed with LF_N at a 1:1 molar ratio with respect to PA monomer, purified over S200 gel filtration in 20 mM Tris, 150 mM NaCl, pH 8.0, and tested for homogeneity by MS (**Supplementary Fig. 2b**). The protein complex was incubated with 20 mM ATP on ice for 10 min and then mixed 1:1 with well solution (13–17% (w/v) polyethylene glycol with average molecular weight 3,000 Da (PEG-3000), 100 mM cacodylic acid, 200 mM $MgCl_2$, pH 6.7–7.3) and then subjected to hanging-drop vapor-diffusion crystallization. Rectangular prisms grew overnight at 19 °C, maturing to dimensions of 100–300 μm. Crystals were harvested in a 1:1 mixture of well solution and cryoprotectant (50% (v/v) glycerol, 20 mM Tris-Cl, 150 mM NaCl, pH 8) and plunged into liquid N_2. X-ray diffraction data were collected at a wavelength of 1.1159 Å at 100 K on a Quantum 315r CCD detector at beamline 8.3.1 at the Lawrence Berkeley National Laboratory Advanced Light Source[52]. A single crystal, belonging to the $P42_12$ space group, diffracted X-rays to 3.1 Å and had the unit cell dimensions 178.4, 178.4 and 240.4 Å for *a*, *b* and *c*, respectively (**Table 1**). The diffraction data (99.8% complete) were indexed and scaled in HKL2000 (ref. 53).

The $PA_8(LF_N)_4$ complex structure was solved by molecular replacement (MR) using PHASER[54]. The MR search model was a loop-stripped PA dimer from PDB 3HVD[19]. Two PA dimers were found in the asymmetric unit. Rigid-body and TLS refinement using PHENIX[51] produced $F_o - F_c$ electron density consistent with a helical bundle that aligned to LF_N α2, α4, α9 and α10. Rounds of polyalanine-model building in COOT[55] and refinement in PHENIX revealed that the identified polyalanine secondary structure elements aligned well with a model of LF_N (LF residues 51–250 (PDB 1J7N[23])). All of LF_N's secondary-structure elements except the N terminus ($LF_{1–28}$) and the C-terminal helix (α12) were identified and independently refined as rigid bodies to produce the initial model of the PA_2LF_N ternary complex. $LF_{29–50}$ (α1–β1) was manually built extending from α2 (residue 51). Rounds of model building in COOT were followed by coordinate and *B*-factor refinement with noncrystallographic symmetry restraints in PHENIX. Backbone torsion angles were refined using the Torsion Optimization Procedure (TOP) provided by H. Gong, E. Haddadian, T. Sosnick and K. Freed (University of Chicago). Molprobity analysis[56] of the structure shows that 91% of residues are in the favored Ramachandran regions, yielding an overall Molprobity score of 2.88 (87th percentile for a 3.10 (±0.25)-Å-resolution structure). Surface burial calculations and molecular graphics were computed in CHIMERA[57].

Planar lipid bilayer electrophysiology. Planar lipid bilayer currents were recorded using an Axopatch 200B amplifier (Molecular Devices Corp.)[9,19]. Membranes were painted on a 100-μm aperture of a 1-ml white Delrin cup with 3% (w/v) 1,2-diphytanoyl-*sn*-glycerol-3-phosphocholine (Avanti Polar Lipids) in *n*-decane. *Cis* (referring to the side to which the PA oligomer was added) and *trans* chambers were bathed in various buffers as required. By convention, $\Delta\psi \equiv \psi_{cis} - \psi_{trans}$ ($\psi_{trans} \equiv 0$ V), and $\Delta pH \equiv pH_{trans} - pH_{cis}$.

PA channel binding was measured under asymmetric KCl solutions buffered in 10 mM potassium phosphate ($[added\ KCl]_{cis}$ = 100 mM, $[added\ KCl]_{trans}$ = 0 mM, pH = 7.4). Curves of equilibrium current (I) versus ligand concentration [L] were fit to a simple single-binding site model, $I = I_o/(1 + K_d/[L]) + c$, to obtain K_d values, where I_o is the current amplitude and c is an offset. Kinetic binding experiments confirmed the equilibrium K_d values (**Supplementary Methods**). The K_d values for Δn LF_N were deduced in equilibrium competition experiments with WT LF_N-PA channel complexes (**Supplementary Fig. 6d,e**).

LF_N translocation experiments were conducted as described previously[9] using a universal pH bilayer buffer system (UBB: 10 mM oxalic acid, 10 mM phosphoric acid, 10 mM MES, 1 mM EDTA and 100 mM KCl) at symmetrical pH 5.6, 40-mV $\Delta\psi$ (**Supplementary Methods**). LF translocation experiments were carried out similarly except that a 1.3-unit ΔpH and 20-mV $\Delta\psi$ were applied during translocation. The pH of the UBB in the *cis* and *trans* chambers was adjusted to apply the proton gradient (pH_{cis} 6.1, pH_{trans} 7.4). Relative translocation efficiency ($\varepsilon_{MUT}/\varepsilon_{WT}$) and $\Delta\Delta G^{\ddagger}$ were calculated for each mutant. A separate protocol (**Supplementary Methods**) was devised to analyze the PA R178A mutant because of LF's rapid dissociation from the channel.

Equilibrium unfolding titrations. Guanidinium chloride titrations were performed on Δn LF_N in 10 mM sodium phosphate, 0.75 M trimethylamine *N*-oxide, pH 7.5, 20 °C as described[9,26]. Each titration point was probed by circular dichroism (CD) spectroscopy at 222 (±2) nm using a Jasco J-810 spectropolarimeter. The CD-probed curves fit to a four-state thermodynamic model ($N \rightleftarrows I \rightleftarrows J \rightleftarrows U$)[26].

Fluorescence anisotropy (FA). The IAEDANS-labeled, cysteine-substituted LF_N residues are listed in **Figure 4e**. FA, *a*, was measured with a FluoroMax-3 spectrofluorometer equipped with moveable linear polarizers at λ_{ex} = 360 (±10) nm, λ_{em} = 510 (±50) nm; fluorescence signals from the parallel ($F_{||}$) and perpendicular ($F_{\perp}$) arrangement of the excitation and emission polarizers were used to calculate FA by $a = F_{||} - F_{\perp} / (F_{||} + 2F_{\perp})$. The FA signal change upon binding PA was not due to nonspecific protein-protein associations, as the LF_N V48C*AEDANS signal change is saturable at a 3:1 stoichiometry (LF_N:PA heptamer) (**Supplementary Fig. 10b**), which is consistent with the number of LF_N molecules that bind to PA_7 (refs. 19,58).

52. MacDowell, A.A. *et al.* Suite of three protein crystallography beamlines with single superconducting bend magnet as the source. *J. Synchrotron Radiat.* **11**, 447–455 (2004).
53. Otwinowski, Z. & Minor, W. Processing of X-ray diffraction data collected in oscillation mode. *Methods Enzymol.* **276**, 307–326 (1997).
54. Storoni, L.C., McCoy, A.J. & Read, R.J. Likelihood-enhanced fast rotation functions. *Acta Crystallogr. D Biol. Crystallogr.* **60**, 432–438 (2004).
55. Emsley, P. & Cowtan, K. COOT: model-building tools for molecular graphics. *Acta Crystallogr. D Biol. Crystallogr.* **60**, 2126–2132 (2004).
56. Davis, I.W. *et al.* MolProbity: all-atom contacts and structure validation for proteins and nucleic acids. *Nucleic Acids Res.* **35**, W375–W383 (2007).
57. Pettersen, E.F. *et al.* UCSF Chimera—a visualization system for exploratory research and analysis. *J. Comput. Chem.* **25**, 1605–1612 (2004).
58. Mogridge, J., Cunningham, K. & Collier, R.J. Stoichiometry of anthrax toxin complexes. *Biochemistry* **41**, 1079–1082 (2002).